Optical and Quantum Electronics (2023) 55:1097
https://doi.org/10.1007/s11082-023-05427-y

Electronic properties and molecular electrostatic potential mapping of edge functionalized GQDs with ZnO, CuO, and TiO_2

Asmaa Ibrahim[1] · **Hend A. Ezzat**[2] · **Mervat Abd El Aal**[1]

Received: 4 January 2023 / Accepted: 13 September 2023 / Published online: 28 September 2023

Abstract

Graphene quantum dots (GQDs) are a cutting-edge material that has excellent electrical, thermal, and mechanical characteristics, as well as minimal toxicity and powerful photoluminescence. These unique properties give GQDs the ability to be used in different electrical, optical, and optoelectronic applications. GQDs with hexagonal and triangular cuts with armchair and zigzag ends (ATRI, AHEX, ZTRI, and ZHEX) were decorated with different metal oxides such as ZnO, CuO, and TiO_2. Metal oxides (MOs) were employed to tune the band gap and electrical properties of GQDs for usage in certain applications. The influence of functionalization on the GQDs electronic properties was examined utilizing HOMO–LUMO orbital distribution and molecular electrostatic potential (MESP) mapping calculations. The model structures were calculated using density functional theory (DFT: B3LYP/LanL2DZ). The band gap energies of AHEX C42, ZHEX C54, ATRI C60, and ZTRI C46 were found to be 3.508, 2.886, 3.177, and 0.305 eV, respectively. The findings show that addition of MOs increases the total dipole moment (TDM) while decreasing the band gap energy ΔE. The most effective metal MO on GQDs band gap and electronic properties was TiO_2, which enhanced the band gap energy ΔE for AHEX C42-TiO_2, ZHEX C54-TiO_2, ATRI C60-TiO_2, and ZTRI C46-TiO_2 to 0.391, 0.530, 0.287, and 0.250 eV, respectively. Accordingly, GQDs seem to be excellent for certain applications. Accordingly, GQDs functionalized with ZnO could be used for sensors, due to their increased responsiveness and energy gap variation while GQDs functionalized with TiO_2 is excellent to be applied as optoelectronic materials.

Keywords GQDs · Metal oxides · TDM · MESP · Band gap energy · Sensors · Optoelectronic materials

---

✉ Hend A. Ezzat
hend.ezzat@nriag.sci.eg

[1] Physics Department, Faculty of Women for Arts, Science and Education, Ain Shams University, Cairo 11757, Egypt

[2] Nano Unite, Space Lab, Solar and Space Research Department, National Research Institute of Astronomy and Geophysics (NRIAG), Helwan, Cairo 11421, Egypt

1 Introduction

Carbon nanomaterials (CNMs) such as carbon nanotubes, fullerenes, nanoporous carbon, carbon nanofibers, graphene (G), and G derivatives have recently attracted a lot of attention. CNMs have great focus due to their significant properties, such as extraordinary surface properties, including large surface area, porosity, high chemical stability, low density, easy modification, and controlled structural behavior (Gusain et al. 2020). Accordingly, CNMs are employed in a variety of applications, including nanoscale electronic components (Ajayan and Tour 2007), energy storage (Sun et al. 2017), batteries (Wu et al. 2019), and conversion systems (Raman et al. 2013). CNMs can also help with environmental applications, including sensing (Li et al. 2019a) and pollution removal (Jun et al. 2018). Furthermore, CNMs have important biological applications such as drug delivery (Wong et al. 2013), electrochemical biosensors (Kour et al. 2020), and disease monitoring, treatment, and control (Mitragotri et al. 2015).

The most significant CNMs are G-based nanomaterials, which are applied in different fields of application such as super capacitors (Yang et al. 2019), antimicrobial agents (Anand et al. 2019), and environmental remediation applications (Wang et al. 2019a). GQDs are one of the most significant recent G-based materials, known as zero-dimensional (0D) nanomaterials, with unique electronic, fluorescent, photoluminescent, optical, and biological properties. These properties have sparked increased interest in GQDs to be used in a variety of applications, including sensing and bio-imaging, solar cell applications, and several other applications (Li et al. 2019b). Because GQDs have various constraints that limit their applicability, adjusting the characteristics of GQDs is critical if the material is to be applied in a variety of applications (Chung et al. 2021). GQDs may be functionalized to change their optical, chemical, and electrical characteristics, allowing them to be employed in a variety of applications (Ghaffarkhah et al. 2022).

GQDs with functionalization, substitution, and/or doping have lately become a significant stage in developing improved materials with the qualities necessary to fulfil application requirements (Nande et al. 2023). Edge-functionalized GQDs also have significantly improved power conversion efficiency and have recently been used in solar cell applications (Tian et al. 2018; Mahalingam et al. 2021). Also, the sensing properties of GQDs with hydroxyl groups OH on the edges have been improved for gas sensing applications (Sharma and Jha 2019). Furthermore, substituting nitrogen (N) into GQDs is utilized to modify both their chemical compositions and their different crystalline forms. N-doped GQDs are particularly well suited for optical, sensing, energy, and biological applications (Arunragsa et al. 2020). The charge transport layer for a high-rate and long-lasting $Li_4Ti_5O_{12}$-based Li-ion battery is N-functionalized GQDs. N-functionalized GQDs serve as a stable charge transport and protection layer for Li-ion batteries, resulting in high transport performance and a long life (Gu et al. 2020). Furthermore, GQD functionalization using MOs has received a lot of interest for modifying the physical, chemical, thermal, and stability characteristics (Khan et al. 2019).

Accordingly, GQDs functionalization with NiO microspheres recorded great improvements to be applied for lithium storage applications (Yin et al. 2018). Additionally, amino-functionalized GQDs had a strong positive response to Fe^{3+} detection (Wang et al. 2019b). Chitosan/carboxyl-functionalized GQDs thin films have improved optical and surface plasmon resonance sensing characteristics and could detect Hg^{2+} (Ramdzan et al. 2019).

Theoretical molecular modeling is a powerful tool for studying the physical, chemical, and biological properties of chemical compounds, particularly nanomaterials (Bayoumy et al. 2020). Molecular modeling has different levels of theories utilized for studying chemical compounds and reactions' properties (Budyka 2019; Abdelsalam et al. 2019). One of the most accurate theoretical approaches is DFT, which studies the properties of nanomaterials and provides indications close to what an experiment does (Hegazy et al. 2022; Omar et al. 2022). DFT calculations are commonly used in investigating the properties of CNMs and G-based nanomaterials, and their decorations (Ezzat et al. 2019a, 2018). Moreover, molecular structure could be studied and provided with significant information about compounds and their interactions by calculating infrared (IR) spectrum theoretically, which confirms the expressed-value IR result (El-Mansy et al. 2021; Refaat et al. 2019).

Because of the importance of G and GQDs, and their functionalized derivatives, the current study was conducted to investigate the electronic properties of different GQDs cuts functionalized with various MOs, including ZnO, CuO, and TiO_2. DFT simulations were performed to study the change in electronic properties and charge distribution as a result of functionalization. Electronic properties were studied in terms of TDM, band gap energy (ΔE), HOMO–LUMO orbital distribution, and MESP mapping parameters. Moreover, the theoretical IR spectrum was computed and compared to the experimentally obtained ATR-FTIR spectrum of the prepared GQDs.

2 Calculation details

Following DFT: B3LYP/ LanL2DZ (Becke 1993; Lee et al. 1988; Vosko et al. 1980) calculations, the four different forms of GQDs were interacted with metal oxides such as ZnO, CuO, and TiO_2. Models were processed with the GAUSSIAN09 (Frisch et al. 2010) package at the Molecular Modeling and Spectroscopy Laboratory, National Research Centre, Egypt. TDM, ΔE, HOMO–LUMO orbital distribution, and MESP mapping were conducted on the studied model structures to investigate the electronic properties of the chosen GQDs and how they interacted with ZnO, CuO, and TiO_2.

3 Results and discussion

3.1 Building model molecule

According to achive the porpouse of these work, functionalization of GQDs were considered with kind of MOs for tuning electronic properties and band gap. Functionalization of GQDs with MOs make it able to be used in specific applications (Guo et al. 2021). GQDs is a zero-band gap material with edge effect which has the ability to be enhanced with variety of organic and inorganic materials according to the target application (Kadian et al. 2021). According to Boltzmann statistics, the total quantity and type of electronic charge carriers in a MO are a consequence of the band gap energy. Electronic conduction is classified as n-hopping or p-hopping depending on whether the primary charge carriers are electrons or holes(Mather and Martinez-Arias 2007).

Accordingly, ZnO and TiO_2 (as n-type)with a direct wide bandgap and a relatively large exciton binding energy at room temperature which is attractive for sensing and optoelectronic applications (Schmidt-Mende and MacManus-Driscoll 2007; Sadaf et al. 2011) were chosen beside CuO with narrow band gap, variety of chemo-physical properties, low cost, and high surface area to volume ratio (Sansonov 1982) a good candidate for sensing and uniqe optical and electrical properties (Filipic and Cvelbar 2012). Accordingly, the interaction mechanizm were supposed to be GQDs with hexagonal and triangular edges were decorated with ZnO, CuO, and TiO_2. The symbols ATRI and AHEX correspond to triangular and hexagonal GQDs with armchair endings, respectively. In addition, symbols ZTRI and ZHEX stand for triangular and hexagonal GQDs with zigzag ends, respectively. The impact of MOs decoration on the electronic properties of GQDs was investigated in terms of TDM, HOMO–LUMO orbital distribution, and MESP mapping calculations. The four forms of GQDs, ATRI, AHEX, ZTRI, and ZHEX, were enhanced by connecting the MOs under investigation to one edge of each of the different forms. Figures 1a, 2a, 3a, and 4a demonstrate the model structures of the four forms of GQDs: ATRI, AHEX, ZTRI, and ZHEX, which contain 42, 54, 60 and 46 carbon atoms. All forms were used that the edge morphology have different response with functionalization beside the effect of edge cutting morphology on tuning the electrical properties and band gap (Li et al. 2011; Abdelsalam et al. 2018).

Each of those forms are decorated with the different MOs including ZnO, CuO, and TiO_2. The interaction of ZnO, CuO and TiO_2 with GQDs occurs once from the metal atom (as in Fig. 1b) and once from the oxygen atom (as in Fig. 1c) (Ezzat et al.

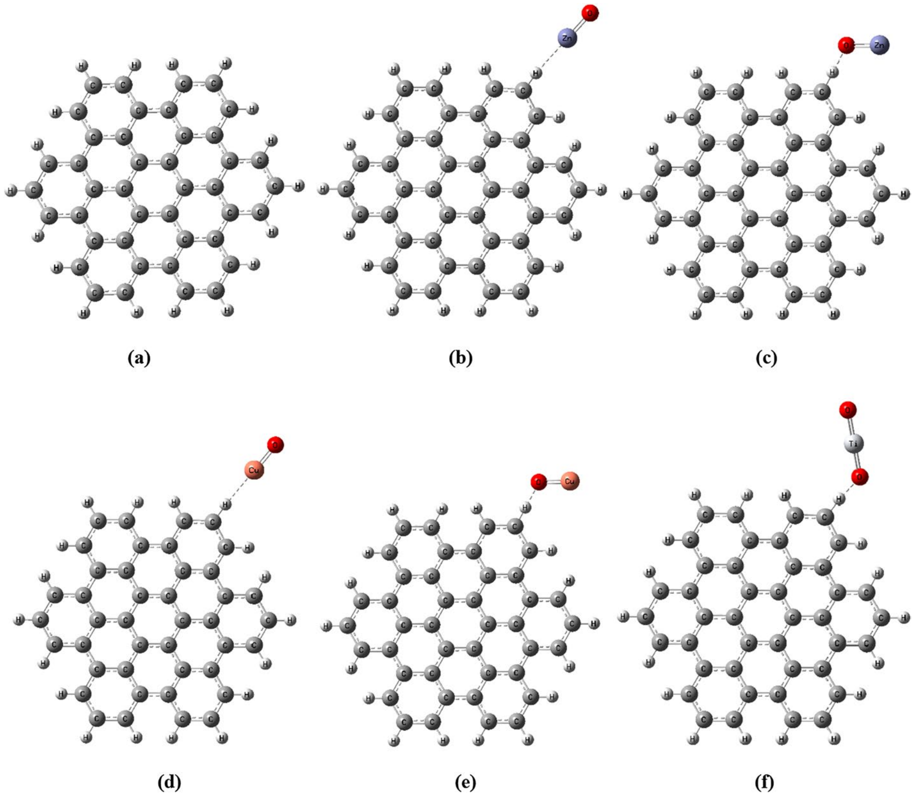

Fig. 1 Optimized structure of AHEX C42 and the interaction of AHEX C42 with metal oxides as: **a** AHEX C42, **b** AHEX C42-ZnO, **c** AHEX C42-OZn, **d** AHEX C42-CuO, **e** AHEX C42-OCu, **f** AHEX C42-OTiO

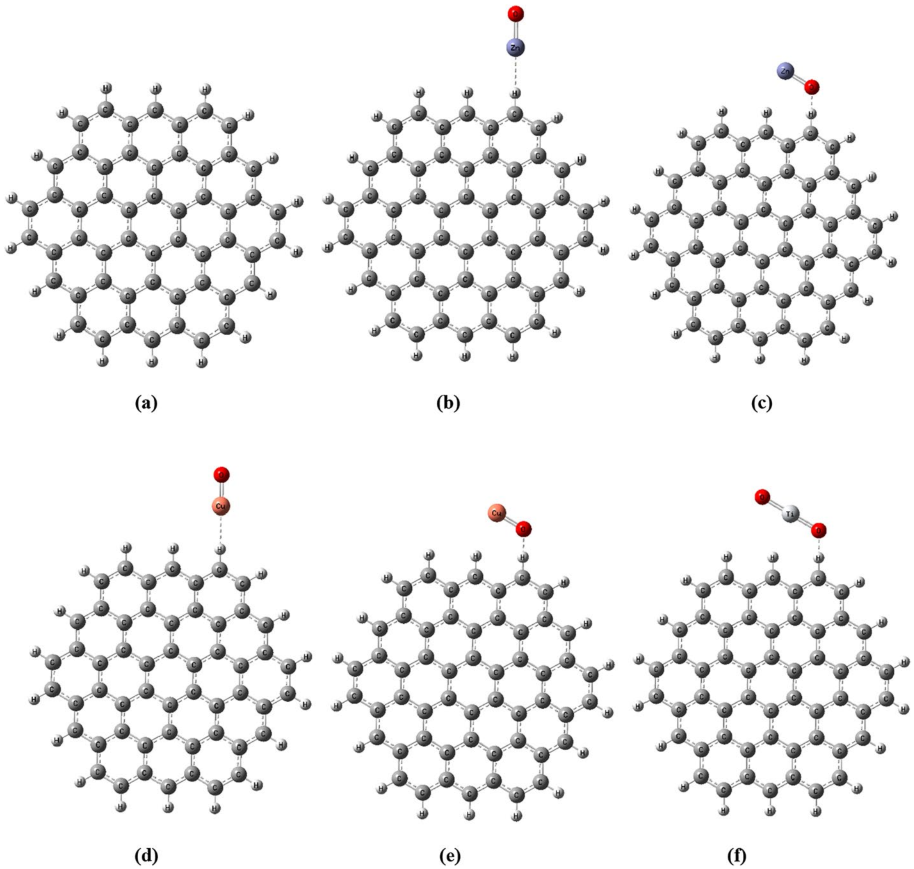

Fig. 2 Optimized structure of ZHEX C54 and the interaction of ZHEX C54 with metal oxides as: **a** ZHEX C54, **b** ZHEX C54-ZnO, **c** ZHEX C54-OZn, **d** ZHEX C54-CuO, **e** ZHEX C54-OCu, **f** ZHEX C54-OTiO

2019b). GQDs models' edge functionalized with ZnO, CuO, and TiO_2 were optimized at B3LYP/ LanL2DZ level of theory.

3.2 TDM and HOMO–LUMO orbital distribution

TDM and HOMO -LUMO band gap energy (Δ E) are the most important indicators of electrical characteristics as well as responsiveness and probably of the investigated interactions (Ezzat et al. 2018; Badry et al. 2018; Ibrahim 2009). Moreover, it is commonly known that the indicator of enhancement of chemical systems correlates with greater TDM and lower calculated (ΔE) (Ibrahim and Mahmoud 2009; Politzer et al. 1985). Accordingly, the simulated model structures were optimized to calculate the TDM, HOMO–LUMO orbital distribution and bandgap energy.

The HOMO–LUMO orbital distribution of AHEX C42 GQD and its interaction with ZnO, CuO, and TiO_2 are shown in Fig. 5. The AHEX C42 HOMO–LUMO orbital dispersion as shown in Fig. 5a is distributed uniformly over the surface and edges. The HOMO–LUMO orbitals were rearranged after metal oxides were attached to the AHEX

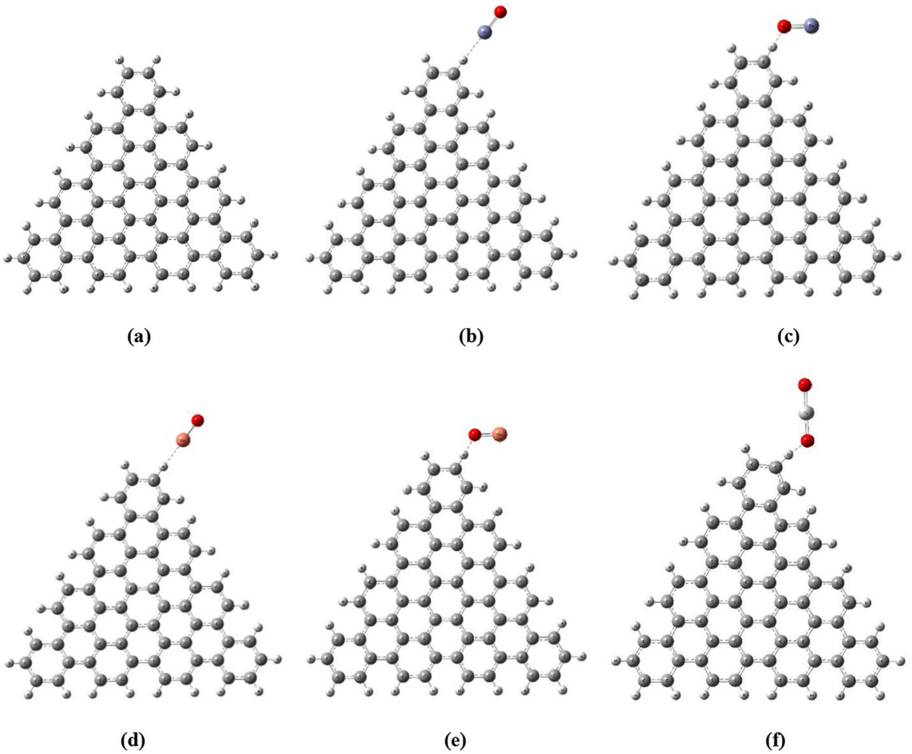

Fig. 3 Optimized structure of ATRI C60 and the interaction of ATRI C60 with metal oxides as: **a** ATRI C60, **b** ATRI C60-ZnO, **c** ATRI C60-OZn, **d** ATRI C60-CuO, **e** ATRI C60-OCu, **f** ATRI C60-OTiO

C42 GQD. As in Fig. 5 b and f the HOMO orbitals were switched with LUMO orbitals in the same position for AHEX C42 GQD interacted with ZnO and TiO_2 while in case of OZn (Fig. 5c) the orbitals were rearranged around the carbon ring arms. In the case of AHEX C42 GQD with CuO (Fig. 5d), the HOMO–LUMO dispersion is concentrated in the center of the surface flower like, while for AHEX C42 GQD with OCu (Fig. 5e) having the same features with the HOMO orbitals were switched with LUMO orbitals in the same position. As listed in Table 1, TDM of AHEX C42 increased from 0.000 Debye to 8.771, 6.045, 7.281, 4.387 and 2.881 for AHEX C42 and its interaction with ZnO, OZn, CuO, OCu and OTiO, respectively. At the same time, ΔE decreased from 3.508 eV to 1.859, 0.777, 2.231, 1.466 and 0.391 eV for AHEX C42 and its interaction with ZnO, OZn, CuO, OCu and OTiO, respectively. Accordingly, the most enhanced structure of these studied models was found to be AHEX C42-OTiO and AHEX C42-OZn which have the smallest band gap value and the most probable and stable interaction. Accordingly, all interacted MOs enhanced the electrical properties of AHEX C42 GQD and enhanced the sensitivity and reactivity of it.

In addition, as illustrated in Fig. 6a, the HOMO–LUMO orbital dispersion for GQD ZHEX C54 is spread throughout the surface and edges. The GQD ZHEX C54 interacted with ZnO, OZn and TiO_2 (Fig. 6b, c, and f), the HOMO–LUMO orbital shape were changed and move slightly to dispersion to be redistributed in the edges with some orbitals on the surface. For GQD ZHEX C54 interaction with CuO and OCu (Fig. 6d and e), the

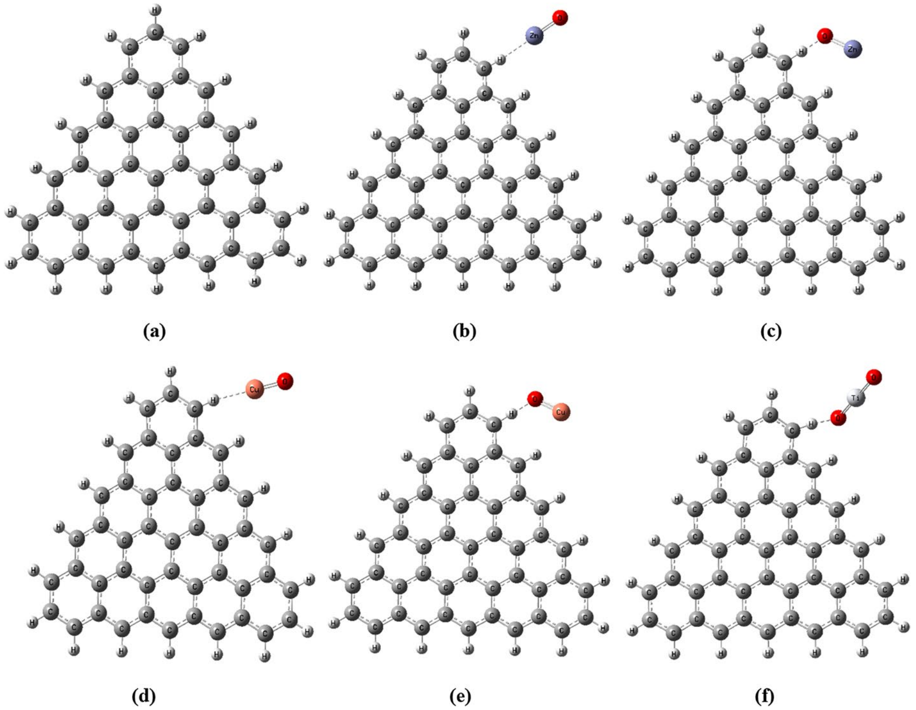
(a) (b) (c) (d) (e) (f)

Fig. 4 Optimized structure of ZTRI C46 and the interaction of ZTRI C46 with metal oxides as: **a** ZTRI C46, **b** ZTRI C46-ZnO, **c** ZTRI C46-OZn, **d** ZTRI C46-CuO, **e** ZTRI C46-OCu, **f** ZTRI C46-OTiO

HOMO–LUMO orbital was localized on the edges and disappeared from the center which means that the electrons were localized on the edges. TDM of ZHEX C54 improved from 0.000 Debye to 9.455, 4.635, 7.718, 3.595, and 5.505 when it interacted with ZnO, OZn, CuO, OCu, and OTiO, as shown in Table 2. Simultaneously, ΔE dropped from 2.886 eV to 1.589, 0.632, 1.833, 1.171, and 0.530 eV, respectively. As a result, ZHEX C54-OZn and ZHEX C54-OTiO were the most upgraded structure. Also, for this form of GQD all the MOs enhanced the electrical characteristics and band gap.

The HOMO–LUMO orbital distribution for GQD ATRI C60 is illustrated in Fig. 7a. The HOMO–LUMO orbital for GQD ATRI C60 is distributed throughout the surface and edges. The interaction of ATRI C60 with ZnO makes slight ineffective change as shown in Fig. 7b. In case of OZn and TiO_2 (Fig. 7c and f) caused the HOMO–LUMO orbital to be reallocated in the surface's center and switched around the carbon ring edge. While because of the interaction of ATRI C60 with CuO (Fig. 7d), the HOMO–LUMO orbital was concentrated on the central sector, which appears as a rectangular shape. When ZHEX C54 interacted with ZnO, OZn, CuO, OCu, and OTiO, its TDM increased from 0.000 Debye to 9.214, 5.710, 7.507, 4.183, and 4.472, as shown in Table 3. At the same time, ΔE decreased from 3.177 eV to 1.634, 0.764, 2.014, 1.306, and 0.287 eV, respectively. Consequently, the ZHEX C54-OZn and ZHEX C54-OTiO were the most improved structure.

Finally, Fig. 8 illustrates the HOMO–LUMO orbital distribution for GQD ZTRI C46 and GQD ZTRI C46 interacted with metal oxides. From the Fig. 8a, the GQD ZTRI C46 HOMO–LUMO orbital is spread across the edge of the structure. As ZTRI C46 interacts

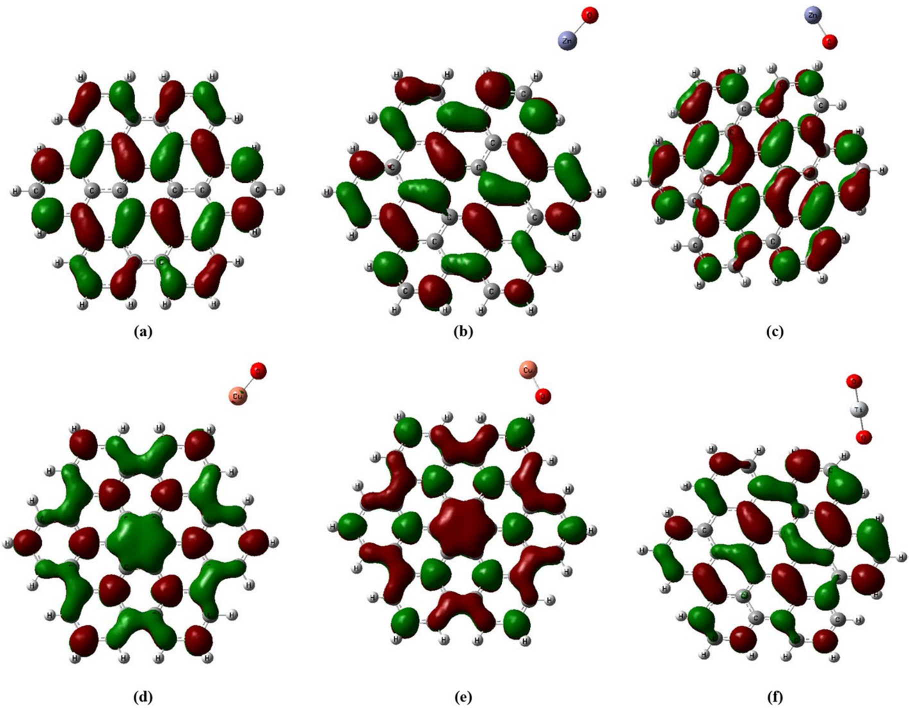

Fig. 5 HOMU-LUMO orbital distribution of AHEX C42 and the interaction of AHEX C42 with metal oxides using DFT:B3LYP/ LanL2DZ as: **a** AHEX C42, **b** AHEX C42-ZnO, **c**AHEX C42-OZn, **d** AHEX C42-CuO, **e** AHEX C42-OCu, **f** AHEX C42- OTiO

Table 1 DFT: B3LYP/LanL2DZ calculated TDM as Debye and ΔE as eV for AHEX C42 and AHEX C42 interacted with metal oxides

Structure	TDM (Debye)	ΔE (eV)
AHEX C42	0.000	3.508
AHEX C42-ZnO	8.771	1.859
AHEX C42-OZn	6.045	0.777
AHEX C42-CuO	7.281	2.231
AHEX C42-OCu	4.387	1.466
AHEX C42-OTiO	2.881	0.391

with ZnO (through Zn atom or O atom) and TiO_2 (Fig. 8 b, c and e), the HOMO–LUMO orbital was reallocated at the edge surrounding the MO. In the case of ZTRI C46- CuO and ZTRI C46-OCu (Fig. 8 d and e), the HOMO–LUMO orbital was spread on all surfaces. As shown in Table 4, when ZTRI C46 interacted with ZnO, OZn, CuO, OCu, and OTiO, its TDM increased from 2.211 Debye to 9.246, 5.713, 7.727, 3.688, and 9.044 Debye, respectively. ΔE of ZTRI C46 decreased from 0.305 eV to 0.291, 0.260, and 0.250 eV for the interaction with ZnO, OZn, and OTiO, while it is increased to 1.190, and 0.659 eV for the interaction with CuO and OCu respectively. From these results,

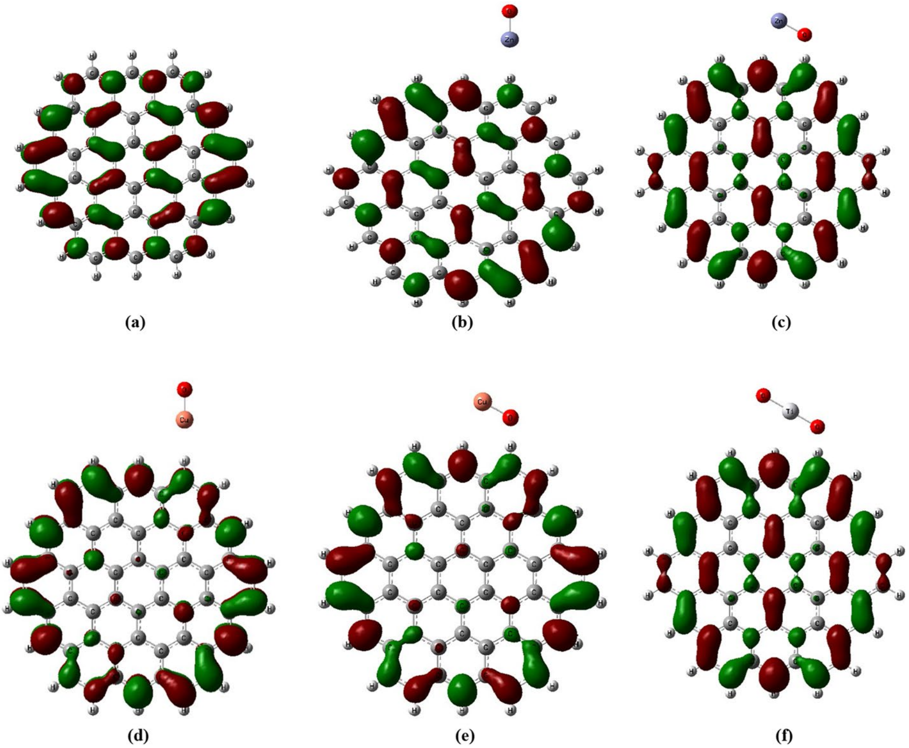
(a) (b) (c)

(d) (e) (f)

Fig. 6 HOMU-LUMO orbital distribution of ZHEX C54 and the interaction af ZHEX C54 with metal oxides using DFT:B3LYP/ LanL2DZ as: **a** ZHEX C54 **b** ZHEX C54-ZnO **c** ZHEX C54-OZn **d** ZHEX C54-CuO **e** ZHEX C54-OCu **f** ZHEX C54-OTiO

Table 2 DFT:B3LYP/ LanL2DZ calculated TDM as Debye and ΔE as eV for ZHEX C54 and the interaction of ZHEX C54 with metal oxides

Structure	TDM (Debye)	ΔE (eV)
ZHEX C54	0.000	2.886
ZHEX C54-ZnO	9.455	1.589
ZHEX C54-OZn	4.635	0.632
ZHEX C54-CuO	7.718	1.833
ZHEX C54-OCu	3.595	1.171
ZHEX C54-OTiO	5.505	0.530

ZTRI C46-OTiO was found to be the most electronically enhanced structure as it has the highest TDM and the lowest ΔE.

3.3 Molecular electrostatic potential (MESP)

MESP is useful because it can relate the impacts of the total charge distribution to electronegativity, dipole moment, partial charge, and the chemical reactivity sides of the molecule. MESP investigates the reactivity of the components of intermolecular interaction to characterize

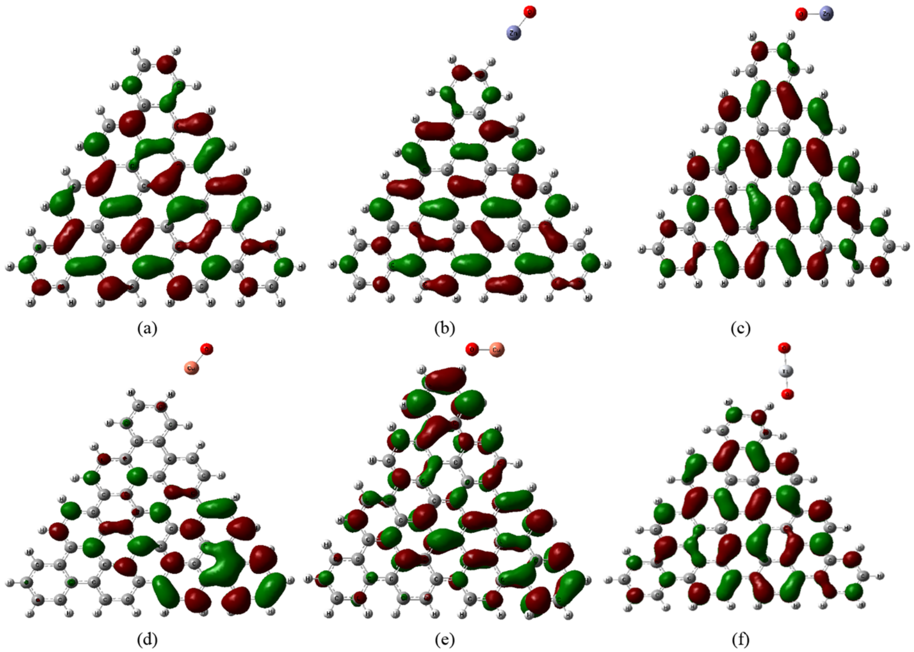

Fig. 7 HOMU-LUMO orbital distrbution of ATRI C60 and the interaction of ATRI C60 with metal oxides using DFT:B3LYP/ LanL2DZ as: **a** ATRI C60, **b** ATRI C60-ZnO, **c** ATRI C60-OZn, **d** ATRI C60-CuO, **e** ATRI C60-OCu, **f** ATRI C60 –OtiO

Table 3 DFT:B3LYP/ LanL2DZ calculated TDM as Debye and ΔE as eV for ATRI C60 and the interaction of ATRI C60 with metal oxides

Structure	TDM (Debye)	ΔE (eV)
ATRI C60	0.000	3.177
ATRI C60-ZnO	9.214	1.634
ATRI C60-OZn	5.710	0.764
ATRI C60-CuO	7.507	2.014
ATRI C60-OCu	4.183	1.306
ATRI C60-OTiO	4.472	0.287

the reactivity and stability of chemical structures. As a result, the electrostatic potential of the molecule is a suitable reference for determining the reactivity of the molecules to positively or negatively charged substances (Lu and Chen 2020). On the molecule's surface, different MESP values are shown in different colours in the following order: red > orange > yellow > green > blue. Highest potential is commonly found in red regions, whereas the most unattractive potential is found in blue. The colour difference indicated as red on the MESP surface is corresponding to a negative area, the blue colour refers to a positive region, and the green colour represents zero electrostatic potential. As shown in Figs. 9 and 10 a, the MESP map were perpendicular to the GQD HEX sheets before being decorated with MOs, but after being decorated with MOs, the color map spread in plane with the GQD sheet shown

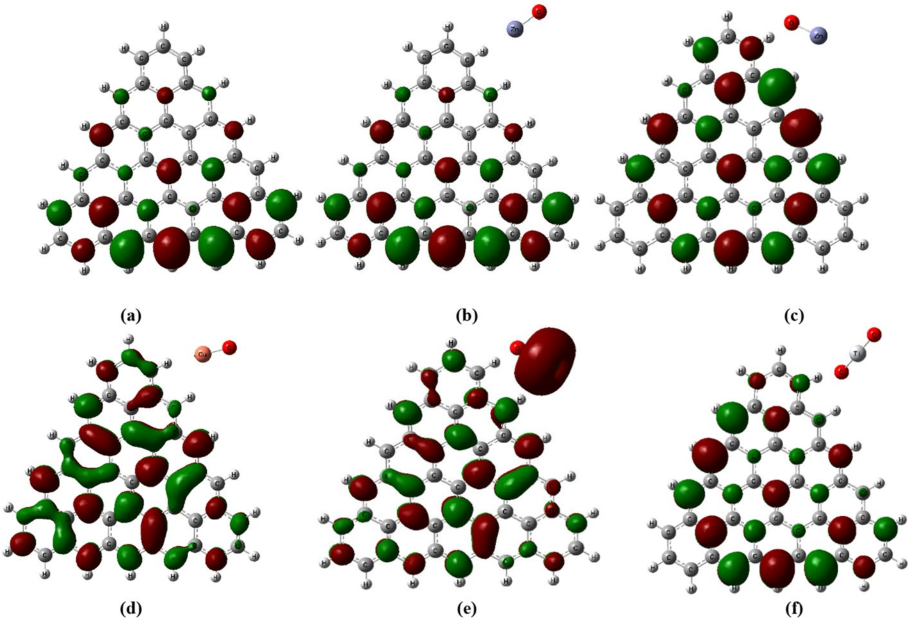

Fig. 8 HOMO–LUMO orbital distribution of ZTRI C46 and the interaction of ZTRI C46 with metal oxides using DFT:B3LYP/ LanL2DZ as: **a** ZTRI C46, **b** ZTRI C46-ZnO, **c** ZTRI C46-OZn, **d** ZTRI C46-CuO, **e** ZTRI C46-OCu, **f** ZTRI C46-OTiO

Table 4 DFT:B3LYP/ LanL2DZ calculated TDM as Debye and ΔE aseV for ZTRI C46 and ZTRI C46 interacted with metal oxides

Structure	TDM (Debye)	ΔE (eV)
ZTRI C46	2.211	0.305
ZTRI C46-ZnO	9.246	0.291
ZTRI C46-OZn	5.713	0.260
ZTRI C46-CuO	7.727	1.190
ZTRI C46-OCu	3.688	0.659
ZTRI C46-OTiO	9.044	0.250

in Figs. 9 and 10 b–f. The map was spread in a horizontal plane with yellow colour in the case of GQD TRI sheets, as shown in Figs. 11a and 12a. In addition, in the case of ZnO and TiO_2, red colour increased around the MO, but in the case of CuO, the red colour increased over the whole GQD sheet, as shown in Figs. 11 and 12 d and e. According to MESP calculations, GQD interaction with MO activated its surface. And the most active MO was CuO, followed

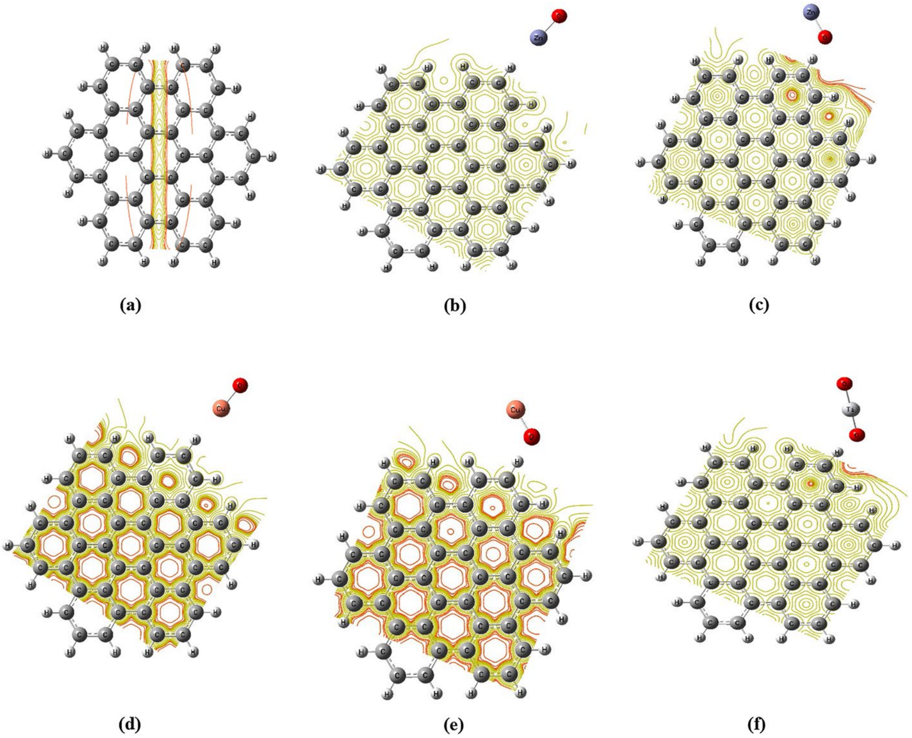

Fig. 9 MESP of AHEX C42 and the interaction of AHEX C42 with metal oxides using DFT:B3LYP/ LanL2DZ as: **a** AHEX C42, **b** AHEX C42-ZnO, **c**AHEX C42-OZn, **d**AHEX C42-CuO, **e**AHEX C42-OCu, **f**AHEX C42- OTiO

by TiO_2. This indicates that MO activates the GQD surface, and enhances its electronic properties and detection sensitivity, with GQD ZTRI C46 being the most enhanced GQDs form. As a result, GQDs decorated with CuO may be utilized as a sensing material, whereas GQDs decorated with TiO_2 could be used in electrical devices and/or as optoelectronic material.

3.4 GQDs Characterization

3.4.1 IR results of GQDs theoretical and experimental

DFT:B3LYP at the LanL2DZ basis set was used to determine the IR frequencies of GQDs (AHEX C42, ZHEX C54, ATRI C60, and ZTRI C46). The theoretical IR spectrum of GQDs of various forms was computed and compared to the experimentally obtained ATR-FTIR spectrum of the produced GQDs. Figure 13 demonstrates the computed IR spectra of GQDs of various forms, as well as the ATR-FTIR absorbance spectrum of manufactured GQDs (14). Table 5 compare the theoretical IR frequencies of GQDs with experimental data, including the various forms of AHEX C42, ZHEX C54, ATRI C60, and ZTRI C46. After correction using the basis set scale factor, the

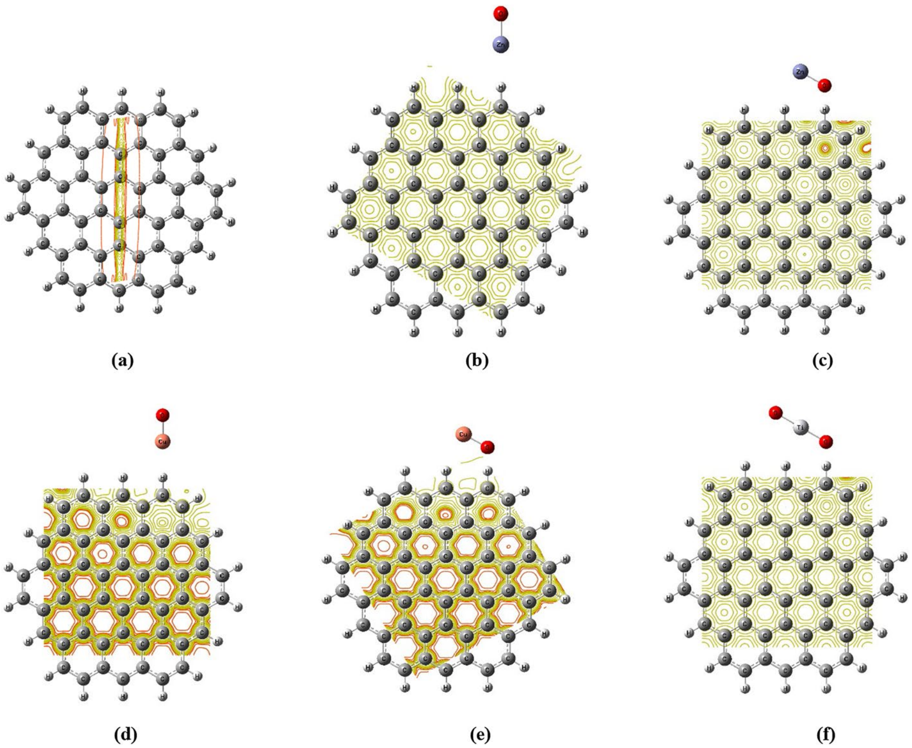

Fig. 10 MESP of ZHEX-C54 and the interaction of ZHEX-C54 with metal oxides using DFT:B3LYP/ LanL2DZ as: **a** ZHEX C54, **b** ZHEX C54-ZnO, **c** ZHEX C54-OZn, **d** ZHEX C54-CuO, **e** ZHEX C54-OCu, **f** ZHEX C54-OTiO

theoretical IR information was provided. Table 5 demonstrates the fingerprint of the molecular structure of GQDs. The main characteristic bands representing GQDs, which are attributed to the bands observed around 1636 cm^{-1} can be attributed to C–C stretching vibrations (Dager et al. 2019). In addition, the band at 1189 cm^{-1} can be assigned to in-plane C–H bending (Tang et al. 2017). Therefore, the presence of C–C in-plane symmetric stretching can be assigned to the band at 1049 cm^{-1}. Finally, the bands around ~884 and ~579 cm^{-1} represent C-H out-of-plane bending (Danial et al. 2022). The characteristic bands of the GQDs theoretical IR spectra of several kinds of GQDs are almost the same as in the experimental spectrum (Fig. 13 and 14).

3.4.2 Raman results of GQDs

Figure 15 demonstrates the Raman spectra of GQDs. The main characteristic peaks that represent the pure GQD were observed (Ahirwar et al. 2017) at 1358 and 1605 cm^{-1}. The two observed peaks represent the D and G bands of Raman shifts, and the normal

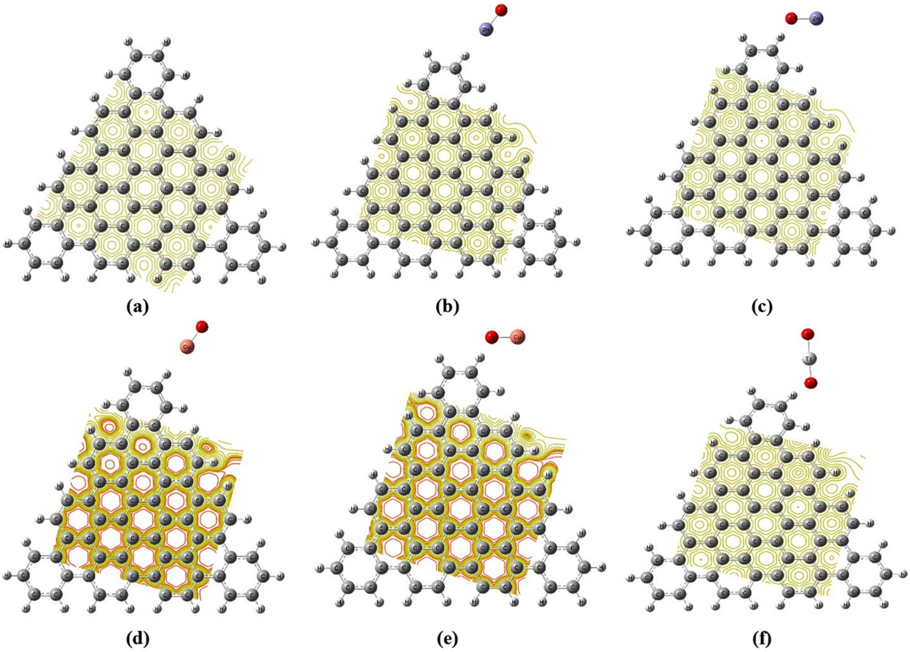

Fig. 11 MESP of ATRI C60 and the interaction of ATRI C60 with metal oxides using DFT:B3LYP/ LanL2DZ as: **a** ATRI C60, **b** ATRI C60-ZnO, **c** ATRI C60-OZn, **d** ATRI C60-CuO, **e** ATRI C60-OCu, **f** ATRI C60 –OtiO

Raman intensity ratio of the D band to the G band was 0.77, an indication for high quality GQD formation with surface defects (Dervishi et al. 2019). The intensity ratio of the D band to the G band, (ID/IG) indicator for the degree of disorder. The D band is a band, confirming the presence of disorder on the edges in the form of sp3 carbons, surface states, or functional groups on the surface of GQDs attributed to bonding and antibonding orbitals. Furthermore, the G band occurs by stretching C–C bonds in the sp2 carbon network (Rajender and Giri 2016).

4 Conclusions

DFT molecular modeling approach was used to study the electronic properties for GQDs and GQDs attached with MOs. The calculations have been carried out for hexagonal and triangular GQDs with armchair and zigzag terminations at B3LYP/LANL2DZ basis set. The attachment of MOs significantly increased the TDM with very high values observed in GQDs attached with ZnO. The increase in the TDM reflects the fact that the given structures are highly reactive with their surrounding media. ΔE was calculated for GQDs and GQDs attached with MOs. The band gap energy of AHEX C42, ZHEX C54, ATRI C60 and ZTRI C46 was found to be 3.508, 2.886, 3.177

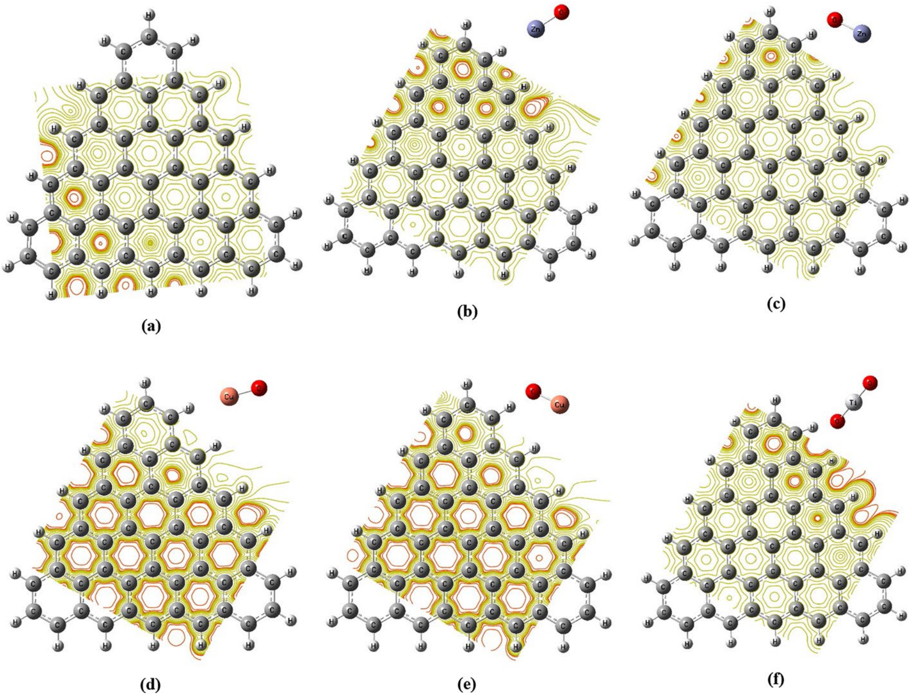

Fig. 12 MESP of ZTRI C46 and the interaction of ZTRI C46 with metal oxides using DFT:B3LYP/ LanL2DZ as: a) ZTRI C46, **b** ZTRI C46-ZnO, **c** ZTRI C46-OZn, **d** ZTRI C46-CuO, **e** ZTRI C46-OCu, **f** ZTRI C46-OTiO

Fig. 13 DFT:B3LYP/ LanL2DZ calculated IR Spectra for GQDs (AHEX C42, ZHEX C54, ATRI C60, and ZTRI C46)

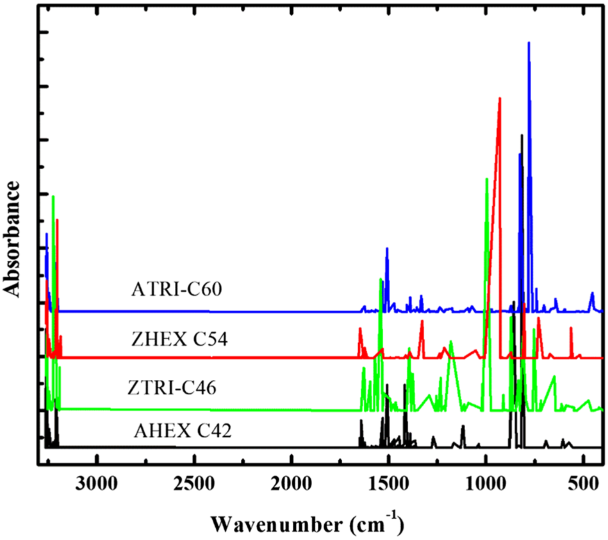

Table 5 The computed IR (Scaled) frequencies of GQDs such as AHEX C42, ZHEX C54, ATRI C60, and ZTRI C46 using the DFT:B3LYP/ LanL2DZ model were compared to the experimental results

Experimental(Cm^{-1})	Theoretical (Cm^{-1})				Assignment
	AHEX C42	ZHEX C54	ATRI C60	ZTRI C46	
33,141	3239	3203	3258–3211	3222	**C-H Stretching**
1636	1630 ~ 1361	1603 ~ 1294	1623–1508	1592 ~ 1377	**C–C Stretching**
1189	1165	1114	1131	1124	**C-H in-plane binding**
1049	1033	1032	1051	1022	**C–C in-plane symmetric Stretching**
884	816	831	827	870	**C-H out-of-plane binding**
579	573	539	545	550	**C-H out-of-plane binding**

The bold is defined as the assignment of the FITR bands

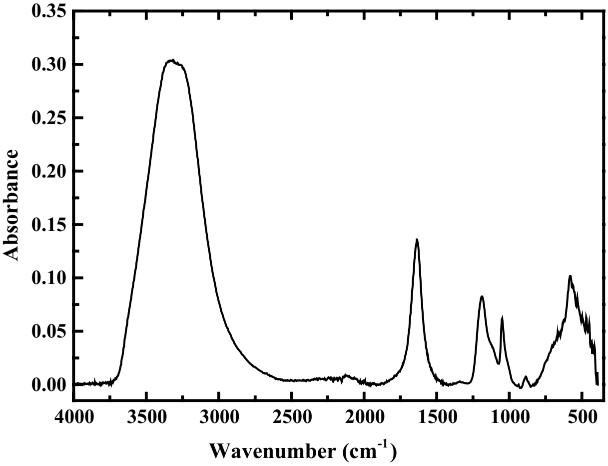

Fig. 14 ATR-FTIR absorbance spectra for GQDs

and 0.305 eV, respectively. The addition of metal oxides decreased the value of ΔE. The most effective metal oxide on GQDs was TiO_2 that enhanced ΔE for AHEX C42-TiO_2, ZHEX C54-TiO_2, ATRI C60-TiO_2 and ZTRI C46-TiO_2 to 0.391, 0.530, 0.287 and 0.250 eV, respectively. MESP was calculated for the studied structures and it was found that MOs activate the GQD surface and enhance its electronic properties and detection sensitivity. GQD ZTRI C46 was found to be the most enhanced GQDs form. As a result, GQDs decorated with CuO may be utilized as a sensing material, where as GQDs decorated with TiO_2 could be used in electrical devices and/or as optoelectronic material. DFT:B3LYP at the LANL2DZ basis set was also used to determine the IR frequencies of GQDs (AHEX C42, ZHEX C54, ATRI C60, and ZTRI C46). The theoretically calculated IR spectra of GQDs of various forms were compared to the experimental

Fig. 15 Raman spectra for GQDs

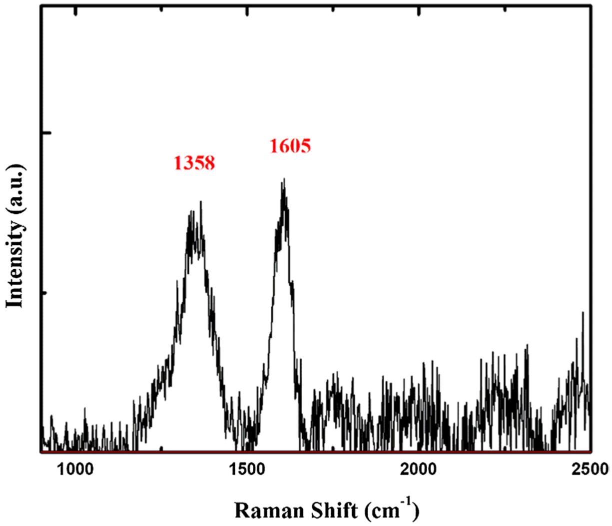

ATR-FTIR spectrum of the produced GQDs, and the comparison indicated that the characteristic bands of theoretical IR spectra of several kinds of GQDs are almost the same as in the experimental spectrum.

Author contributions All authors contributed to the study conception and design. Material preparation, data collection and analysis were performed by Asmaa Ibrahim, Hend A. Ezzat and Mervat Abd El Aal. The first draft of the manuscript was written by Asmaa Ibrahim and all authors commented on previous versions of the manuscript. All authors read and approved the final manuscript.

Funding Open access funding provided by The Science, Technology & Innovation Funding Authority (STDF) in cooperation with The Egyptian Knowledge Bank (EKB). The authors declare that no funds, grants, or other support were received during the preparation of this manuscript.

Data availability The datasets generated during and/or analyzed during the current study are available from the corresponding author on reasonable request.

Declarations

Conflict of interest The authors declare no conflict of interest.

References

Abdelsalam, H., Elhaes, H., Ibrahim, M.A.: Tuning electronic properties in graphene quantum dots by chemical functionalization: Density functional theory calculations. Chem. Phys. Lett. (2018). https://doi.org/10.1016/j.cplett.2018.02.015

Abdelsalam, H., Teleb, N.H., Yahia, I.S., Zahran, H.Y., Elhaes, H., Ibrahim, M.A.: First principles study of the adsorption of hydrated heavy metals on graphene quantum dots. J. Phys. Chem. Solids (2019). https://doi.org/10.1016/j.jpcs.2019.02.014

Ahirwar, S., Mallick, S., Bahadur, D.: Electrochemical method to prepare graphene quantum dots and graphene oxide quantum dots. ACS Omega (2017). https://doi.org/10.1021/acsomega.7b01539

Ajayan, P.M., Tour, J.M.: Nanotube composites. Nature (2007). https://doi.org/10.1038/4471066a

Anand, A., Unnikrishnan, B., Wei, S.C., Chou, C.P., Zhang, L.Z., Huang, C.C.: Graphene oxide and carbon dots as broad-spectrum antimicrobial agents–a minireview. Nanoscale Horiz. (2019). https://doi.org/10.1039/C8NH00174J

Arunragsa, S., Seekaew, Y., Pon-On, W., Wongchoosuk, C.: Hydroxyl edge-functionalized graphene quantum dots for gas-sensing applications. Diam. Relat. Mater.Relat. Mater. (2020). https://doi.org/10.1016/j.diamond.2020.107790

Badry, R., Ghanem, A.S., Ahmed, H., Fahmy, A., Elhaes, H., Refaat, A., Ibrahim, M.: Effect of Li, Na, K, Be, Mg and Ca on the electronic properties, geometrical parameters of carboxylic acids. Biointerface Res Appl Chem **8**, 3657–3660 (2018)

Bayoumy, A.M., Refaat, A., Yahia, I.S., Zahran, H.Y., Elhaes, H., Ibrahim, M.A., Shkir, M.: Functionalization of graphene quantum dots (GQDs) with chitosan biopolymer for biophysical applications. Opt. Quantum Electron. (2020). https://doi.org/10.1007/s11082-019-2134-z

Becke, A.D.: Density-functional thermochemistry III. The role of exact exchange. J. Chem. Phys. **98**, 5648–5652 (1993). https://doi.org/10.1063/1.464913

Budyka, M.F.: Semiempirical study on the absorption spectra of the coronene-like molecular models of graphene quantum dots. Spectrochim. Acta A Mol. Biomol. Spectrosc. (2019). https://doi.org/10.1016/j.saa.2018.09.007

Chung, S., Revia, R.A., Zhang, M.: Graphene quantum dots and their applications in bioimaging, biosensing, and therapy. Adv. Mater. (2021). https://doi.org/10.1002/adma.201904362

Dager, A., Uchida, T., Maekawa, T., Tachibana, M.: Synthesis and characterization of mono-disperse carbon quantum dots from fennel seeds: photoluminescence analysis using machine learning. Sci. Rep. (2019). https://doi.org/10.1038/s41598-019-50397-5

Danial, W.H., Abdullah, M., Bakar, M.A.A., Yunos, M.S., Ibrahim, A.R., Iqbal, A., Adnan, N.N.: The valorisation of grass waste for the green synthesis of graphene quantum dots for nonlinear optical applications. Opt. Mater. (2022). https://doi.org/10.1016/j.optmat.2022.112853

Dervishi, E., Ji, Z., Htoon, H., Sykora, M., Doorn, S.K.: Raman spectroscopy of bottom-up synthesized graphene quantum dots: size and structure dependence. Nanoscale (2019). https://doi.org/10.1039/C9NR05345J

El-Mansy, M.A., Bayoumy, A.M., Ezzat, H., El-Sayed, N., Elhaes, H., Osman, O., Ibrahim, A.: Modeling the Effect of Hydration on the Electronic and Vibrational Properties of AZT. Biointerface Res Appl Chem. (2021). https://doi.org/10.33263/BRIAC112.92539265

Ezzat, H., Badry, R., Yahia, I.S., Zahran, H.Y., Elhaes, H., Ibrahim, M.A.: Mapping the molecular electrostatic potential of carbon nanotubes. Biointerface Res. Appl. Chem. **8**, 3539–3542 (2018)

Ezzat, H., Badry, R., Yahia, I.S., Zahran, H.Y., Ibrahim, A., Elhaes, H., Ibrahim, M.: Mapping the molecular electrostatic potential of fullerene. Egypt. J. Chem. (2019a). https://doi.org/10.21608/EJCHEM.2019.5353.1472

Ezzat, H.A., Hegazy, M.A., Nada, N.A., Ibrahim, M.A.: Effect of nano metal oxides on the electronic properties of cellulose, chitosan and sodium alginate. Biointerface Res Appl. Chem. (2019b). https://doi.org/10.33263/BRIAC94.143149

Filipic, G., Cvelbar, U.: Copper oxide nanowires: a review of growth. Nanotechnol. (2012). https://doi.org/10.1088/0957-4484/23/19/194001

Frisch, M. J., Trucks, G. W., Schlegel, H. B., Scuseria, G. E., Robb, M. A., Cheeseman, J. R., Scalmani, G. Barone, V., Mennucci, B., Petersson, G. A., Nakatsuji, H., Caricato, M., Li, X., Hratchian, H. P., Izmaylov, A. F., Bloino, J., Zheng, G., Sonnenberg, J. L., Hada, M., Ehara, M., Toyota, K., Fukuda, R., Hasegawa, J., Ishida, M., Nakajima, T., Honda, Y., Kitao, O., Nakai, H., Vreven, T., Montgomery Jr., J.A., Peralta, J. E., Ogliaro, F., Bearpark, M., Heyd, J. J., Brothers, E., Kudin, K. N., Staroverov, V. N., Keith, T., Kobayashi, R.; Normand, J., Raghavachari, K., Rendell, A., Burant, J.C., Iyengar, S.S., Tomasi, J., Cossi, M., Rega, N., Millam, J.M., Klene, M., Knox, J.E., Cross, J.B., Bakken, V., Adamo, C., Jaramillo, J., Gomperts, R., Stratmann, R.E., Yazyev, O., Austin, A.J., Cammi, R., Pomelli, C., Ochterski, J.W., Martin, R.L., Morokuma, K., Zakrzewski, V.G., Voth, G.A., Salvador, P., Dannenberg, J.J., Dapprich, S., Daniels, A.D., Farkas, O., Foresman, J.B., Ortiz, J.V., Cioslowski, J., Fox, D.J.: Gaussian 09, Revision C.01, Gaussian, Inc., Wallingford, CT, (2010).

Ghaffarkhah, A., Hosseini, E., Kamkar, M., Sehat, A.A., Dordanihaghighi, S., Allahbakhsh, A., Arjmand, M.: Synthesis, applications, and prospects of graphene quantum dots: a comprehensive review. Small (2022). https://doi.org/10.1002/smll.202102683

Gu, S., Hsieh, C.T., Yuan, C.Y., Gandomi, Y.A., Chang, J.K., Fu, C.C., Juang, R.S.: Fluorescence of functionalized graphene quantum dots prepared from infrared-assisted pyrolysis of citric acid and urea. J. Lumin.Lumin. (2020). https://doi.org/10.1016/j.jlumin.2019.116774

Guo, R., Li, L., Wang, B., Xiang, Y., Zou, G., Zhu, Y., Ji, X.: Functionalized carbon dots for advanced batteries. Energy Stor. Mater. (2021). https://doi.org/10.1016/j.ensm.2021.01.020

Gusain, R., Kumar, N., Ray, S.S.: Recent advances in carbon nanomaterial-based adsorbents for water purification. Coord. Chem. Rev.. Chem. Rev. (2020). https://doi.org/10.1016/j.ccr.2019.213111

Hegazy, M.A., Ezzat, H.A., Yahia, I.S., Zahran, H.Y., Elhaes, H., Gomaa, I., Ibrahim, M.A.: Effect of CuO and Graphene on PTFE microfibers: experimental and modeling Approaches. Polymers (2022). https://doi.org/10.3390/polym14061069

Ibrahim, M.: Molecular modeling and FTIR study for K, Na, Ca and Mg coordination with organic acid. J. Comput. Theor. Nanosci.Comput. Theor. Nanosci. (2009). https://doi.org/10.1166/jctn.2009.1094

Ibrahim, M., Mahmoud, A.-A.: Computational notes on the reactivity of some functional groups. J. Comput. Theor. Nanosci.Comput. Theor. Nanosci. (2009). https://doi.org/10.1166/jctn.2009.1205

Jun, L.Y., Mubarak, N.M., Yee, M.J., Yon, L.S., Bing, C.H., Khalid, M., Abdullah, E.C.: An overview of functionalised carbon nanomaterial for organic pollutant removal. J. Ind. Eng. Chem. (2018). https://doi.org/10.1016/j.jiec.2018.06.028

Kadian, S., Sethi, S.K., Manik, G.: Recent advancements in synthesis and property control of graphene quantum dots for biomedical and optoelectronic applications. Mater. Chem. Front. (2021). https://doi.org/10.1039/D0QM00550A

Khan, F., Oh, M., Kim, J.H.: N-functionalized graphene quantum dots: Charge transporting layer for high-rate and durable $Li_4Ti_5O_{12}$-based Li-ion battery. J. Chem. Eng. (2019). https://doi.org/10.1016/j.cej.2019.03.161

Kour, R., Arya, S., Young, S.J., Gupta, V., Bandhoria, P., Khosla, A.: Recent advances in carbon nanomaterials as electrochemical biosensors. J. Electrochem. Soc.Electrochem. Soc. (2020). https://doi.org/10.1149/1945-7111/ab6bc4

Lee, C., Yang, W., Parr, R.G.: Development of the Colic-Salvetti correlation-energy formula into a functional of the electron density. Phys. Rev. B **37**, 785 (1988). https://doi.org/10.1103/physrevb.37.785

Li, Y., Wei, Y., Shi, G., Xian, Y., Jin, L.: Facile synthesis of leaf-like CuO nanoparticles and their application on glucose biosensor. Electroanalysis (2011). https://doi.org/10.1002/elan.201000343]

Li, X., Ping, J., Ying, Y.: Recent developments in carbon nanomaterial-enabled electrochemical sensors for nitrite detection. TrAC, Trends Anal. Chem. (2019a). https://doi.org/10.1016/j.trac.2019.01.008

Li, M., Chen, T., Gooding, J.J., Liu, J.: Review of carbon and graphene quantum dots for sensing. ACS Sens. (2019b). https://doi.org/10.1021/acssensors.9b00514

Lu, T., Chen, Q.: van der Waals potential: an important complement to molecular electrostatic potential in studying intermolecular interactions. J. Mol. Model. (2020). https://doi.org/10.1007/s00894-020-04577-0

Mahalingam, S., Manap, A., Omar, A., Low, F.W., Afandi, N.F., Chia, C.H., Abd Rahim, N.: Functionalized graphene quantum dots for dye-sensitized solar cell: key challenges, recent developments and future prospects. Renewable Sustainable Energy Rev. (2021). https://doi.org/10.1016/j.rser.2021.110999

Mather, G.C., Martinez-Arias, A.: Transport properties and Oxygen Handling in “Synthesis, Properties and Applications of Oxide Nanoparticles” (Rodríguez, J.A., Fernández-García, M; Eds.). Whiley: N.J. (2007).

Mitragotri, S., Anderson, D.G., Chen, X., Chow, E.K., Ho, D., Kabanov, A.V., Xu, C.: Accelerating the translation of nanomaterials in biomedicine. ACS Nano (2015). https://doi.org/10.1021/acsnano.5b03569

Nande, A., Tiwari, A., Raut, S., Dhoble, S. J.: Graphene and graphene oxide: Application in luminescence and solar cell. In: Functional Materials from Carbon, Inorganic, and Organic Sources. Woodhead Publishing (2023). https://doi.org/10.1016/B978-0-323-85788-8.00004-5.

Omar, A., Bayoumy, A.M., Aly, A.A.: Functionalized graphene oxide with chitosan for dopamine biosensing. J. Funct. Biomater. (2022). https://doi.org/10.3390/jfb13020048

Politzer, P., Laurence, P.R., Jayasuriya, K.: Molecular electrostatic potentials: an effective tool for the elucidation of biochemical phenomena. Environ. Health Perspect.Perspect. (1985). https://doi.org/10.1289/ehp.8561191

Rajender, G., Giri, P.K.: Formation mechanism of graphene quantum dots and their edge state conversion probed by photoluminescence and Raman spectroscopy. J. Mater. Chem. C (2016). https://doi.org/10.1039/C6TC03469A

Raman, K.V., Kamerbeek, A.M., Mukherjee, A., Atodiresei, N., Sen, T.K., Lazić, P., Moodera, J.S.: Interface-engineered templates for molecular spin memory devices. Nature (2013). https://doi.org/10.1038/nature11719

Ramdzan, N.S.M., Fen, Y.W., Omar, N.A.S., Anas, N.A.A., Daniyal, W.M.E.M.M., Saleviter, S., Zainudin, A.A.: Optical and surface plasmon resonance sensing properties for chitosan/carboxyl-functionalized graphene quantum dots thin film. Optik (2019). https://doi.org/10.1016/j.ijleo.2018.10.071

Refaat, A., Ibrahim, M.A., Elhaes, H., Badry, R., Ezzat, H., Yahia, I.S., Shkir, M.: Geometrical, vibrational and physical properties of polyvinyl chloride nanocomposites: molecular modeling approach. J. Theor. Comput. Chem.Theor. Comput. Chem. (2019). https://doi.org/10.1142/S0219633619500378

Sadaf, J.R., Israr, M.Q., Nur, O., Willander, M., Ding, Y., Wang, Z.L.: The correlation between radiative surface defect states and high color rendering index from ZnO nanotubes. Nanoscale Res. Lett. (2011). https://doi.org/10.1186/1556-276X-6-513

Sansonov, G.V.: The oxide handbook. IFI/Plenum Press, New York (1982)

Schmidt-Mende, L., MacManus-Driscoll, J.L.: ZnO – nanostructures, defects, and devices. Mater. Today (2007). https://doi.org/10.1016/S1369-7021(07)70078-0

Sharma, V., Jha, P.K.: Enhancement in power conversion efficiency of edge-functionalized graphene quantum dot through adatoms for solar cell applications. Sol. Energy Mater. Sol. Cells (2019). https://doi.org/10.1016/j.solmat.2019.04.030

Sun, H., Mei, L., Liang, J., Zhao, Z., Lee, C., Fei, H., Duan, X.: Three-dimensional holey-graphene/niobia composite architectures for ultrahigh-rate energy storage. Science (2017). https://doi.org/10.1126/science.aam5852

Tang, Q., Zhu, W., He, B., Yang, P.: Rapid conversion from carbohydrates to large-scale carbon quantum dots for all-weather solar cells. ACS Nano (2017). https://doi.org/10.1021/acsnano.6b06867

Tian, P., Tang, L., Teng, K.S., Lau, S.P.: Graphene quantum dots from chemistry to applications. Mater. Today Chem. (2018). https://doi.org/10.1016/j.mtchem.2018.09.007

Vosko, S.H., Wilk, L., Nusair, M.: Accurate spin-dependent electron liquid correlation energies for local spin density calculations: a critical analysis. J. Phys. **58**, 1200–1211 (1980). https://doi.org/10.1139/p80-159

Wang, Y., Pan, C., Chu, W., Vipin, A.K., Sun, L.: Environmental remediation applications of carbon nanotubes and graphene oxide: Adsorption and catalysis. J. Nanomater.Nanomater. (2019a). https://doi.org/10.3390/nano9030439

Wang, R., Fan, H., Jiang, W., Ni, G., Qu, S.: Amino-functionalized graphene quantum dots prepared using high-softening point asphalt and their application in Fe3+ detection. Appl. Surf. Sci. (2019b). https://doi.org/10.1016/j.apsusc.2018.10.104

Wong, B.S., Yoong, S.L., Jagusiak, A., Panczyk, T., Ho, H.K., Ang, W.H., Pastorin, G.: Carbon nanotubes for delivery of small molecule drugs. Adv. Drug Deliv. Rev.Deliv. Rev. (2013). https://doi.org/10.1016/j.addr.2013.08.005

Wu, Z., Wang, Y., Liu, X., Lv, C., Li, Y., Wei, D., Liu, Z.: Carbon-nanomaterial-based flexible batteries for wearable electronics. Adv. Mater. (2019). https://doi.org/10.1002/adma.201800716

Yang, Z., Tian, J., Yin, Z., Cui, C., Qian, W., Wei, F.: Carbon nanotube-and graphene-based nanomaterials and applications in high-voltage supercapacitor: a review. Carbon (2019). https://doi.org/10.1016/j.carbon.2018.10.010

Yin, X., Chen, H., Zhi, C., Sun, W., Lv, L.P., Wang, Y.: Functionalized graphene quantum dot modification of yolk–shell NiO microspheres for superior lithium storage. Small (2018). https://doi.org/10.1002/smll.201800589